Accurate and Consistent Microwave Observations of Venus and their Implications

Bryan J. Butler
National Radio Astronomy Observatory [1]
P. O. Box O
Socorro, NM 87801

Paul G. Steffes, Shady H. Suleiman
School of Electrical and Computer Engineering
Georgia Institute of Technology
Atlanta, GA 30332–0250

Marc A. Kolodner
Johns Hopkins University
Applied Physics Laboratory
Laurel, MD 20723–6099

Jon M. Jenkins
SETI Institute
NASA Ames Research Center
Moffett Field, CA 94035

submitted to Icarus on August 31, 2000
resubmitted on June 13, 2001

30 pages; 4 figures (1 color); 5 tables.

[1] The National Radio Astronomy Observatory is a facility of the National Science Foundation operated under cooperative agreement by Associated Universities, Inc.

Proposed running head: Venus Microwave Spectrum

Please address all editorial correspondence to:

Bryan J. Butler
National Radio Astronomy Observatory
P. O. Box O
Socorro, NM 87801

phone: 505-835-7261
FAX: 505-835-7027
email: bbutler@nrao.edu

Abstract

We present observations of Venus at six frequencies: 1.385, 1.465, 4.86, 8.44, 14.94, and 22.46 GHz. These were obtained with the Very Large Array (VLA), and calibrated in a consistent fashion. The brightness temperature of Venus at the six frequencies is derived, and compared to a model which includes the emission from the atmosphere, surface, and subsurface of Venus. A single set of model inputs can fit the higher frequency data, where the emission comes mostly from the atmosphere. At the lower frequencies, where emission comes mostly from the surface and subsurface, the model has difficulty reproducing the measurements, and the lowest two frequencies are not reproduced well at all. Improvements in this model over past models include new formalisms for the microwave opacity of SO_2 and H_2SO_4, and incorporation of measured topography and surface characteristics from Magellan. The inputs to the model which best fits the higher frequency data include a relatively warm temperature profile (more consistent with the Mariner V occultation temperature profile than that from the Pioneer-Venus sounders), a disk averaged abundance of gaseous H_2SO_4 of 1-2.5 ppm at and just below the lower cloud layer and an average SO_2 abundance of $\lesssim 50$ ppm for all altitudes below the cloud layers. This H_2SO_4 abundance is consistent with the values inferred from Magellan occultations, taking into account the differences between equatorial and polar locations (Jenkins and Steffes 1991; Kolodner and Steffes 1998). The SO_2 abundance in the lower atmosphere is in agreement with earlier results of Steffes *et al.* (1990), but much lower than the 180 ppm inferred from the Pioneer sounder probe (Oyama *et al.* 1980) or the 130 ppm inferred from infrared observations (Bézard *et al.* 1993). Models with as much as 130 ppm of SO_2 only fit the measurements if the atmosphere is nearly completely devoid of H_2SO_4 and the temperature profile which is much warmer than that measured by the Pioneer-Venus probes is used.

Keywords: Venus, Radio Observations, Radiative Transfer

Introduction

Since telescopes were first pointed at the heavens, Venus has been the object of intense scrutiny by intrigued astronomers. For some time, it was not known that what was being observed was not the surface of the planet, but actually bright clouds at the top of a very thick atmosphere. In fact, at optical wavelengths, no radiation from the surface or atmosphere below the clouds, either scattered or emitted, can be observed. However, they may be probed at the much longer wavelengths of the radio portion of the spectrum. Thus, it was not until the development of receivers and telescopes sensitive to radiowaves (in the late 1950's and early 1960's) that the thick lower atmosphere and surface of Venus were probed (see Barrett and Staelin [1964] for a good review of early radio wavelength observations of Venus). Since that time, many such observations have been undertaken, allowing our knowledge of these regions of Venus to continually progress. It has recently become known that there are also windows in the infrared, through which the lower atmosphere, and even the surface, may be probed (Allen and Crawford 1984; Crisp *et al.* 1991; Lecacheux *et al.* 1993). In addition to Earth–based observations, several spacecraft have visited Venus, balloons have been released into its atmosphere (Blamont *et al.* 1995), probes dropped through its atmosphere (Sieff 1991), and landers have been sent to its surface (Vinogradov *et al.* 1976; Florenskii *et al.* 1982). The most recent of those missions was the incredibly successful Magellan spacecraft (Saunders *et al.* 1992), which mapped the surface of the planet in radio emission (Pettengill *et al.* 1992), radar reflection (Pettengill *et al.* 1991), surface roughness (Tyler *et al.* 1992), and topography (Ford and Pettengill 1992) and helped further characterize the atmosphere through a number of radio occultation experiments (Steffes *et al.* 1994; Jenkins *et al.* 1994).

Thus, we have built up over time a body of knowledge of what is happening in the lower atmosphere of Venus. The atmosphere is very thick, reaching $\sim$ 90 bars at the surface. It is comprised mostly of CO_2 ($\sim$ 96%), with a small amount of N_2 ($\sim$ 4%), and trace amounts of SO_2, CO, H_2O, H_2SO_4, and other gases. Because of the thick atmosphere, and because CO_2 is such a good greenhouse gas, the temperature at the surface is very hot, near 750 K. There are several cloud and haze layers in the atmosphere, at altitudes between about 30 and 90 km above the surface, comprised mostly of sulfuric acid (H_2SO_4). However, important questions still remain unanswered regarding the lower atmosphere of Venus. One of these questions is the abundance of sulfur-bearing molecules, and their possible spatial (both vertical and horizontal) and temporal variation. For example, the abundance of SO_2 at the cloud tops (near 70 km) decreased sharply from 1978 to 1980, then decreased slowly until 1986, but has held relatively steady since that time (Esposito *et al.* 1988; Na *et al.* 1990; Zasova *et al.* 1993; Na *et al.* 1994). This is in direct contrast to observations which indicate that the abundance of SO_2 in the deep atmosphere (near 40 km) has remained nearly constant over that same time period (Bézard *et al.* 1993). Because SO_2 provides significant opacity at microwave wavelengths, very accurate measurements at those wavelengths, combined with accurate lab measurements of its opacity, and a radiative transfer model for the atmosphere, may be used to provide constraints on its abundance in the lower atmosphere. Observations performed in 1987 (Steffes *et al.* 1990) indicated that the abundance of SO_2 in the deep atmosphere was much lower than measured by the Pioneer sounder (Oyama *et al.* 1980), or subsequently in

the infrared by Bézard *et al.* (1993). These differences have not been resolved. Occultation experiments also seem to indicate that there is some spatial and temporal variation in the abundance of H_2SO_4 in the lower atmosphere (Jenkins and Steffes 1991). Note however that very little is currently known about the vertical distribution of SO_2 and H_2SO_4 in the lower atmosphere.

Recently, accurate lab measurements have provided much improved formalisms for the microwave opacity of SO_2 and H_2SO_4 vapor (Suleiman *et al.* 1996; Kolodner and Steffes 1998). Therefore, we have undertaken a series of interoferometric radio wavelength observations of Venus from the Very Large Array, in an attempt to further understand the lower atmosphere of Venus, and especially the inventory and variability (spatial and temporal) of sulfur-bearing molecules. This paper will describe the first portion of the reduction of those data, including the data collection and calibration, and present average brightness temperature values and their implications. Detailed analysis of maps made from the data will be presented in a future paper (Jenkins *et al.* 2001, in preparation). There is a well developed history of interferometric observations of Venus (see e.g., Clark and Spencer 1964; Clark and Kuz'min 1965; Berge and Greisen 1969; Hall and Branson 1971; Berge *et al.* 1972; Sinclair *et al.* 1972; Muhleman *et al.* 1973; Pettengill *et al.* 1988; Gurwell *et al.* 1995), but we feel that the improved sensitivity of the observations, the fact that they are based upon a common calibration scale, and the new laboratory information on the microwave opacities of SO_2 and H_2SO_4, warrant this investigation.

Observations and Data Reduction

All observations described herein were undertaken at the Very Large Array (VLA) of the National Radio Astronomy Observatory. The VLA is a collection of 27 radio antennas, each 25 m in diameter, spread out in a Y shape on the plains of San Augustin, New Mexico. Each of the pairs of antennas acts as a two element interferometer, and the combination of all of these individual interferometers allows for the reconstruction of the full sky brightness distribution, in both dimensions (Thompson *et al.* 1991).

The VLA is tunable in eight discrete frequency bands from about 70 MHz to about 50 GHz. We present in this paper measurements in five of these bands: L (1.385 and 1.465 GHz), C (4.86 GHz), X (8.44 GHz), U (14.94 GHz), and K (22.46 GHz). In all of our observations, we observed in the continuum mode, which essentially provides measurements of the total intensity (Stokes I) with an equivalent bandwidth of $\sim$ 92 MHz [2]. The exception is the two L-band frequencies, where the IF's are not averaged together, resulting in an effective bandwidth of $\sim$ 65 MHz. The observations were undertaken on different days in April of 1996 and January of 1999. Table I lists the dates, along with other experiment and ephemeris information. The VLA was in its C configuration for all of the experiments, with maximum

←**Tab. I**

[2]The VLA receivers actually operate in the two orthogonal circular polarizations, with $\sim$ 46 MHz bandwidth in each polarization. Since for Venus, we expect the two circular polarizations to have equal intensity, they are combined into a total intensity polarization (Stokes I), for an effective increase of $\sqrt{2}$ to the bandwidth, yielding $\sim$ 65 MHz equivalent bandwidth. There are also two independent IF's (frequency tuners/filters), which are averaged together for another $\sqrt{2}$ effective increase in bandwidth, to $\sim$ 92 MHz.

physical antenna separation of $\sim$ 3 km. Calibration of the data proceeded in the normal fashion for VLA data, in the AIPS reduction package (http://www.cv.nrao.edu/aips/). Observations of an unresolved secondary calibrator (see Table II) were used to remove long timescale (10's of minutes) atmospheric and system fluctuations in the data. For all of the observations the absolute flux density scale was set with an observation of 3C286, with assumed flux density values listed in Table II for the different frequencies. Uncertainties in this flux density scale and implications of the measurements described herein on that scale are discussed later in the paper. ← **Tab. II**

The actual measured quantity of a complex interferometer like the VLA is a sampling of the complex visibility function at the positions of the baselines between each of its antennas. The visibility function is the two dimensional Fourier transform of the sky brightness distribution (see Butler and Bastian [1999] for a description of the expected visibility function for a planet). The individual samples of the visibility function are referred to as visibilities, and are complex quantities (real and imaginary, or amplitude and phase). After the initial calibration, the data product was a set of visibilities for Venus. Two additional steps were necessary to obtain the desired final data product: fully calibrated Venus visibilities. The first was a distance correction. Since, in the longer observations (at 14.94 and 22.46 GHz), the distance of Venus changed by $\sim$ 0.5% during the course of the observations, it was necessary to effectively adjust all of the visibilities to a common distance. A difference of 0.5% in distance would produce an $\sim$ 1% difference in the received flux density. So, we adjusted all of the visibilities as if they had been measured at the furthest distance to Venus. This adjustment is a relatively simple one, and is discussed in detail in Butler and Bastian (1999). This adjustment was not performed for the shorter observations, since the distance variation over those short periods would have produced less than 0.1% variation in the received flux density.

The last step was to apply the technique of self–calibration (Cornwell and Fomalont 1999) to the Venus visibilities themselves. This was done in order to remove short timescale fluctuations (mostly atmospheric) in the data. Self–calibration uses a model of the visibilities to derive antenna based corrections to the visibilities which make them self consistent as a function of time. Both the amplitude and phase may be corrected in this manner, but we corrected only the phase. The model we used was an image made from the visibilities (which was made with the aid of a fit to the visibilities). After self–calibration, the data product is a set of fully calibrated visibilities for Venus. Such visibilities may be used to actually make a map of the sky brightness across the visible disk of Venus. This was done for two of the observations (14.94 and 22.46 GHz), the full description of which is in preparation (Jenkins *et al.* 2001, in preparation). For the shorter observations at the lower frequencies, the coverage of the u-v plane was poor, and mapping was not warranted. For the purposes of this paper, we simply wished to obtain an estimate of the total flux density for each of the frequencies. These flux densities could then be converted into average brightness temperatures for the planet at the observed frequencies.

Deriving the Brightness Temperature

Given a set of visibilities for a planet, we wish to derive the total flux density from the planet, which can then be used to calculate the average brightness temperature. The total flux density at frequency ν from any source is obtained by integrating the brightness B_ν over the source:

$$S_\nu = \int\int_{\text{source}} B_\nu(\theta, \psi)\, d\Omega \quad , \tag{1}$$

where θ and ψ are the angular sky coordinates, and $d\Omega$ is the element of solid angle. This reduces to:

$$S_\nu = \frac{2\,k}{\lambda^2}\,\frac{1}{D^2}\int_0^{2\pi}\int_0^R T_b(r,\psi)\, r\, dr\, d\psi \quad , \tag{2}$$

assuming that we are in the Rayleigh-Jeans portion of the spectrum (safe for the frequencies and temperatures of interest in this paper), and for circular sources (of radius R) of small angular extent. Define the average brightness temperature for the source as:

$$\overline{T_b} = \frac{\int_0^{2\pi}\int_0^R T_b(r,\psi)\, r\, dr\, d\psi}{\pi\, R^2} \quad . \tag{3}$$

Note that the effective brightness temperature across the visible disk of Venus must account for the fact that the cosmic microwave background emission is blocked by the planet (i.e., it is the *contrast* of the brightness temperature of Venus with that from the CMB that we are actually measuring). Accounting for this effect, we have for the effective brightness temperature of the planet:

$$T_b' = T_b - T_{CMB} \quad , \tag{4}$$

where T_b is the true brightness temperature of the planet, and T_{CMB} is the cosmic microwave background temperature (2.7 K). Combining all of this, and solving for the brightness temperature gives:

$$\overline{T_b} = S_\nu\,\frac{\lambda^2}{2\,k}\,\frac{D^2}{\pi\, R^2} \;+\; T_{CMB} \quad . \tag{5}$$

Note that choosing a value for R is somewhat arbitrary, as long as the same value is used when comparing different observations, and when comparing the average brightness temperature obtained from the observations (Eq. 5) to that from a model of the emission (see appendix A). Following the suggestion of Muhleman *et al.* (1979), we use $R = 6120$ km. We obtain the distances for each of the observations from the very accurate JPL planetary ephemeris (which can be accessed on the web through the Horizons system at http://ssd.jpl.nasa.gov/horizons.html).

The total flux density is exactly equivalent to the zero spacing flux density (V_o), or the visibility which would be measured by a pair of antennas with zero separation. The VLA does not measure this quantity explicitly, since it is physically impossible. We must therefore attempt to derive the total flux density from the measured visibilities. In the case where the measured visibilities are at relatively short spacings (where the flux density measured on the shortest spacing is close to the true zero spacing flux density), this can be done with confidence. We do this by fitting (in a least squares sense) the measured visibilities to the

expected visibility function, allowing V_o, and a shape parameter (to allow for limb darkening) to vary. We assume that the planetary disk brightness temperature as projected on the plane of the sky varies as:

$$T_b(r) = T_o \ \cos^n(r/R) \quad , \tag{6}$$

where T_o is the brightness temperature at the disk center, and n is the limb darkening parameter. Then, defining an apparent radial coordinate $\beta = \hat{R}\sqrt{u^2+v^2}$ ($\hat{R}$ is the apparent radius of Venus), the visibility function $V(\beta)$ can be represented by (Butler and Bastian 1999):

$$V(\beta) = V_o \ \Lambda_\xi(z) \quad , \tag{7}$$

where the Λ function of order ξ ($\xi = 1 + n/2$) and argument z ($z = 2\pi\beta$) is given by:

$$\Lambda_\xi(z) = \Gamma(\xi+1)\left(\frac{1}{2}z\right)^{-\xi} J_\xi(z) \quad . \tag{8}$$

Note that we do not use this sky brightness distribution function because we expect it to be the precisely exact one, but rather because it allows the visibility function to be analytically defined while still allowing for some limb darkening. In this sense, it should not be considered as a precise "model" for the Venus brightness temperature distribution, but rather a model for the functional form of the visibility function, which then allows for a good estimation of the total flux density V_o, and the limb darkening n from the measured visibilities. We find these parameters via a non-linear least squares fit, implemented within the AIPS processing package.

We performed these fits on the data set for each of the six frequencies. Figure 1 shows a plot of the real portion of the measured visibilities against β for the 8.44 GHz data, along with the residuals remaining after the fit. The quality of the fit is quite good, remembering that this is a circularly symmetric model (and hence there are expected deviations which occur on size scales roughly equal to the size scale of the disk - hence the "ringing" on that scale in the residuals), and that there are some 35000 individual visibilities (so that if the 1-σ error on each visibility is of order 50 mJy/vis, then the error on V_o is something less than 1 mJy). The data quality and quality of the fits is similar at all frequencies (although for the lowest two frequencies, the measurements are all in the first lobe of the visibility function). Table III shows the resultant fit values of V_o and n for all of the observed frequencies, along with the 1-σ uncertainties for V_o. In all cases, the uncertainty in V_o is dominated by the uncertainty in the absolute flux density calibration scale, as the actual fit uncertainty is extremely small (e.g., the 1-σ uncertainty in the value of V_o for the fit to the 22.46 GHz data was roughly 4 mJy, while even if the uncertainty in the flux density scale is as small as 2%, then the uncertainty in the value of V_o from this is nearly 1.8 Jy). The formal fit uncertainties in n are less than 5×10^{-4} for all frequencies. Also shown in that table is the estimate of the disk averaged brightness temperature $\overline{T_b}$ obtained from Eq. 5. In order to obtain this value it was necessary to make a correction for the resolution of Venus by the primary beam of the VLA antennas, at all frequencies but the lowest two. This is a small correction factor in all of our cases, and is explained in detail in Appendix B. Table III also lists an uncertainty for the final derived disk averaged brightness temperatures. These uncertainties are completely

←**Fig. 1**

←**Tab. III**

dominated by the uncertainty in the absolute flux density calibration scale. We have adopted uncertainties in the flux density scale of 2% for the lowest four frequencies, 3% for 14.94 GHz, and 5% for 22.46 GHz. A full discussion of these errors is beyond the scope of this paper, but this is the current best estimates of these uncertainties at the VLA (R. Perley, personal communication). Our measured brightness temperatures are similar to previously measured ones (see e.g., Steffes *et al.* 1990; Janssen & Klein 1981; Berge *et al.* 1972) but with smaller error bars. We feel that they are superior because of the consistent way in which they were observed and calibrated, because of the intrinsic benefits of interferometric observations, and because of the recent improvements in the flux density scale.

Radiative Transfer Model of Venus

In order to model the total flux density we expect from the planet, we develop a radiative transfer model of the atmosphere and surface of Venus. Along any line of sight which intercepts the atmosphere of Venus, there are three possible sources of radiation: emission from the atmosphere itself, emission from the surface and subsurface, and downward emission from the atmosphere which is reflected from the surface. All three of these mechanisms are treated rigorously in the model, which is described in detail in Appendix A. The major improvements implemented in our model are the new formalisms for the microwave absorption of SO_2 and H_2SO_4, and the use of measured topography and surface properties from Magellan.

The inputs to be varied in the model are the temperature-pressure profile, the SO_2 and H_2SO_4 profiles, and the surface/subsurface parameters. We considered two different temperature-pressure profiles: the one derived from the Pioneer-Venus (PV) probes (Sieff 1991), and the one which is an extrapolation of the profile inferred from occultation measurements of the Mariner V (MV) spacecraft (Muhleman *et al.* 1979). We considered an SO_2 profile which was uniform (at some specified value) at all altitudes below 47 km (the base of the lower cloud layer), decreasing exponentially with a scale height of 3 km above that. We used an input H_2SO_4 profile which was measured by occultation of the Magellan spacecraft near 65° N latitude, with a variable scaling factor. This profile is one from Jenkins *et al.* (1994), but modified with the recent laboratory results of Kolodner and Steffes (1998). This profile has non-zero values between 37 and 51 km above the surface (in and below the lower cloud), and peaks at 4.8 ppm. We allow the scaling factor to multiply the H_2SO_4 profile to a desired peak value. We considered models with either no subsurface contribution or one like that described in Appendix A.

Figure 2 shows the brightness distribution maps which were the result of running the ←**Fig. 2**
model at the four highest frequencies discussed here, and with the input parameters which result in the best fit to our data (see discussion below). Note that these brightness temperature maps were *not* used to derive the final disk averaged brightness temperatures, they were calculated simply to demonstrate visually how the emission changes as the frequency is varied. These 4 maps were created using geometry parameters which are appropriate for the longer wavelength observations on April 30, 1996 (subearth longitude 271.8 E, latitude -5.3, position angle of north pole -4.8, distance .4862 AU). As expected, the shorter wavelengths

are dominated by emission from the atmosphere, while the longer wavelengths are dominated by emission from the surface. The one-way opacities at the disk center for this model are: 5.3 at 22.46 GHz; 2.3 at 14.94 GHz; 0.76 at 8.44 GHz; 0.26 at 4.86 GHz; and 0.024 at 1.385 GHz. The weighting functions (see appendix A) at the disk center peak at a distance above the surface (6052 km) of roughly 20 km at 22.46 GHz and 12 km at 14.94 GHz, and peak at the surface for the lower frequencies. So the central disk brightness temperature is expected to peak between roughly 8 and 3 GHz, as the weighted emission moves down to within the lowest scale height of the atmosphere, then drop slightly at lower frequencies as the emission becomes dominated by the surface (and atmospheric emission becomes negligible). At 22.46 GHz our model emission is very uniform, since less than 1% of the emission comes from the surface and we have assumed a uniform atmosphere here (not varying as a function of latitude and longitude). At 14.94 GHz, the highest peaks on the surface just start to become visible - peeking through the dense lower atmosphere with their lower brightness temperature (due to both lower surface temperature and lower emissivity). At the particular geometry shown in Fig. 2, the tall peak just above and to the right of the disk center is Beta Regio (including Rhea and Theia Montes). At 8.44 GHz, more surface detail is seen, again, with higher topographic points exhibiting lower brightness temperatures. At 4.86 GHz, the atmosphere is nearly transparent, and surface features are distinct.

The subsurface parameters which must be supplied to the model are the heat flux (q), the thermal conductivity (k), the dielectric constants for the upper and lower layers, and an upper layer depth. We varied these values until we achieved reasonable agreement with the 4.86 GHz measured brightness temperature, since it is least affected by the atmosphere (except for the longest wavelengths, which we have trouble modeling - see discussion below). We used a value for the heat flux of $q = 10^{-6}$ cal/cm^2/s. This value is about 2/3 of the Earth's heat flux value, and roughly a factor of two higher than that for Mercury and the Moon (Mitchell and de Pater 1994; Langseth *et al.* 1976). Recent analysis of Magellan data indicates that the heat flux on Venus is similar to that on Mercury and the Moon (McGovern *et al.* 1995), but the uncertainty is still high. We used a value for the thermal conductivity of 10^{-5} cal/s/cm/K. This value for the thermal conductivity is low, given the expected hot temperatures in the upper layer (one might expect something more like 3×10^{-4} cal/s/cm/K [Mitchell and de Pater 1994; Langseth *et al.* 1976]). We do not claim that this low value for the thermal conductivity is necessarily real, or attempt to justify it, except to say that it is required in order to fit the model to the longer wavelength measurements. We used a value of 5×10^{-4} for the loss tangent in the upper layer. This value is somewhat lower than might be considered nominal, but is within reason, given that the specific loss tangent might be as low as 10^{-3} and that the density of the upper layer might be quite high (and if we assume that scattering effects are small at these wavelengths). We use a value of 8.0 for the dielectric constant in the lower layer. This is reasonable if the lower layer is consolidated rock with similar properties to Earth rocks (Campbell and Ulrichs 1969). We used an upper layer depth of 10 meters. This is reasonable, given our understanding of the creation of planetary regoliths and the regolith depth on the Moon (Moore *et al.* 1980; Watkins and Kovach 1973).

Results and Discussion

We ran our model for five of our six observed frequencies (only one of the lower two frequencies was used since they are so similar) while varying the inputs to the model in order to obtain an acceptable fit to the measured brightness temperature values. Table IV shows the resultant brightness temperature values for the model at the five frequencies for various combinations of the sub-cloud SO_2 abundance, the peak H_2SO_4 abundance, the temperature-pressure profile, and inclusion of the subsurface contribution. Also shown in that table is the value of the reduced chi-square: ← **Tab. IV**

$$\chi_r = \frac{\chi}{N} = \frac{1}{N} \sum_{i=1}^{M} \frac{[T_b(\nu_i) - T_{model}(\nu_i)]^2}{\sigma_i^2} \quad , \tag{9}$$

where N is the number of degrees of freedom. We only include the measurements at the higher four frequencies when calculating the reduced chi-square because of the very poor fits to the lowest frequency data point (see discussion below), so $M = 4$ for us. We therefore have four measurements and two unknowns (for a given temperature profile the unknowns are the sub-cloud SO_2 abundance and peak H_2SO_4 abundance), so $N = 2$. A reduced chi-square value around 1 indicates a good fit to the measurements, given the uncertainties.

The first model shown in Table IV (model a) used the PV temperature profile, 130 ppm sub-cloud SO_2 abundance (to match the measured value of Bézard *et al.* 1993), 4.8 ppm peak H_2SO_4, and included the subsurface emission. It is clear that this model is much too cold at all three of the higher frequencies. Also note that the model is much too hot at the lowest frequency. This problem with the longer wavelength measurements and modeling of the brightness temperature spectrum of Venus has been known for some time and discussed at length elsewhere (Schloerb *et al.* 1976; Muhleman *et al.* 1973). We cannot resolve this problem in the context of the model or measurements presented here, i.e., we cannot find any seemingly physically realistic model which can reproduce such a low brightness temperature at the low frequencies (similar to the previous treatments of this problem). This remains an outstanding unsolved problem in planetary radio science. The next three models in Table IV (b-d) show attempts to fit the measured brightness temperatures by reducing the amount of both SO_2 and H_2SO_4 in the atmosphere. A reasonable fit to the measured data is only obtained by nearly completely removing the SO_2 and H_2SO_4 from the atmosphere, something which we know is not sensible. We therefore next concentrate on models using the warmer MV temperature profile.

Models (e) through (j) all use the warmer MV temperature profile. Once again, similar to model (a), when 130 ppm sub-cloud SO_2 is used along with a peak H_2SO_4 of 4.8 ppm, the model brightness temperatures are too cold at the higher three frequencies. But, unlike the models with the PV temperature profile, it is not necessary to completely remove the SO_2 and H_2SO_4 from the atmosphere to obtain good agreement with the measured brightness temperatures. In fact, as shown by model (h), if the H_2SO_4 is set to 0, and 40 ppm of sub-cloud SO_2 is retained, the model brightness temperatures are generally too hot. Model (g) is the best fit of those shown in Table IV, with 40 ppm sub-cloud SO_2 abundance, a peak H_2SO_4 abundance of 2.4 ppm, and including the subsurface emission. Model run (i)

demonstrates what happens when the subsurface emission is not included. It is very difficult in that case to match the 8.44 and 4.86 GHz measurements, while at the same time still matching the higher frequency measurements, if the subsurface emission is not included. Model run (j) shows the result of using a smaller value for the thermal conductivity in the subsurface (see discussion below).

In order to more fully investigate how sensitive the goodness of fit was to the variation of the SO_2 and H_2SO_4 abundances, we ran the model over an 11 X 11 grid of these values varying from 0 to 4.8 ppm peak H_2SO_4 abundance, and from 0 to 130 ppm sub-cloud SO_2 abundance for each of the two model temperature profiles (also including the subsurface emission). Figure 3 shows the resulting values of reduced chi-square for all of these model runs. Again, it is clear that the colder PV temperature profile does not fit our data well, since a reduced chi-square of $\lesssim 1$ is only obtained if both the SO_2 and H_2SO_4 abundances are near 0. The best fits for the MV temperature profile have sub-cloud SO_2 abundances of $\lesssim 50$ ppm, and peak H_2SO_4 abundances of $\sim$ 1-2.5 ppm. We cannot, however, rule out models which have as much as 130 ppm of sub-cloud SO_2, if the H_2SO_4 abundance is very near 0 and the warmer MV temperature profile is used. ←**Fig. 3**

Figure 4 shows a plot of the measured and model (model (g) from Table IV) disk averaged brightness temperatures at the six frequencies. In addition to our six observed frequencies, we have included in that plot one data point at higher frequency (Ulich *et al.* 1980) and two at lower frequencies (Schloerb *et al.* 1976; Condon *et al.* 1973). We include these older observations because they are either outside the frequency range of the VLA (on the high side) or because no attempt has yet been made to observe Venus with the VLA at those frequencies (on the low side). The model fits the data quite well at the higher frequencies (to better than 2% relative error). One could argue that the model *should* fit the data quite well, given the freedom in varying the model input parameters. But, with the exception of the thermal conductivity, all of the model inputs are quite sensible, and in fact most of them are constrained by other measurements. The necessity of using what seems like an extremely low value for the thermal conductivity (which is really a statement about the *ratio* of the value of the heat flux to the product of the thermal conductivity and specific loss tangent) remains somewhat disconcerting, however. If a more reasonable value of the thermal conductivity is used (10^{-5} rather than 3×10^{-4} cal/s/cm/K), then the model cannot reproduce the high brightness temperatures at 8.44 and 4.86 GHz (see model run (j) in Table IV). This would then imply that there is a problem with the measurements (most likely in the assumed absolute flux density scale) or that there is some other problem with the model (most likely some phenomena which is not included in our present model - e.g., a more detailed treatment of subsurface scattering). There has been some discussion in the past regarding the possibility of an error of the order of 5% in the absolute flux density scale of Baars *et al.* (1977) for the calibrator sources 3C286 and 3C295 (which were essentially the sources used by us to fix the flux density scale) around 8 GHz (Turegano and Klein 1980). We cannot exclude this possibility, but point out that very accurate measurements of these calibrators at the VLA seem to show that the Baars *et al.* values are correct for these secondary calibrators at these frequencies (R. Perley, personal communication). The fact that the two lowest frequencies are so poorly fit by the model also seems to indicate ←**Fig. 4**

that it is not the flux density scale that is the problem (it would have to be off by 10% there, which is highly unlikely), but rather something is not understood about the emission from the venusian surface and subsurface at long wavelength, as mentioned above.

Summary

Using the VLA as an observing tool and by integrating the most modern information on the microwave absorption properties of potential constituents, we have significantly updated our understanding of the microwave emission spectrum of Venus. The measurements are best fit with a relatively warm temperature profile, a disk averaged abundance of gaseous H_2SO_4 of 1-2.5 ppm at and just below the lower cloud layer and an average SO_2 abundance of $\lesssim 50$ ppm for all altitudes below the cloud layers. The H_2SO_4 abundance is consistent with the values inferred from Magellan occultations, taking into account the differences between equatorial and polar locations (Jenkins and Steffes 1991; Kolodner and Steffes 1998). The low SO_2 abundance is in agreement with the earlier results of Steffes *et al.* (1990), but much lower than the 180 ppm inferred from the Pioneer sounder probe (Oyama *et al.* 1980) or the 130 ppm inferred from infrared observations (Bézard *et al.* 1993). The model presented here does not explain the longer wavelength emission from Venus, however, which comes mostly from the surface and subsurface. That problem remains as yet unsolved. A more complete analysis of all of the Venus data taken at the VLA, including detailed maps and observations at shorter and longer wavelengths, will allow for even further understanding of the lower atmosphere of Venus, in particular the sulfur bearing molecules therein, as well as the surface and subsurface of the planet.

Acknowledgements

The measurements described in this paper would not have been possible without the expert help of the staff at the VLA, whose aid was greatly appreciated. Discussions with M. Gurwell, D. Muhleman, and G. Orton were extremely helpful. The aid of K. Desai in implementing the AIPS task to do the non-linear least squares fit (OMFIT) was appreciated. Reviews by G. Pettengill and B. Bézard were appreciated. The NASA Planetary Atmospheres Program supported PGS, SHS, and MAK under NAG5-4190, and JMJ under RTOP 344-33.

Appendix A

In this appendix we develop a model of microwave radiation from Venus. Similar developments can be found in many other places (see e.g., Barrett 1961; Gale and Sinclair 1972; Muhleman *et al.* 1979; Janssen and Klein 1981; Fahd and Steffes 1992; Gurwell *et al.* 1995). We first divide the atmosphere of Venus into N layers. We then trace rays (lines of sight) which intercept the atmosphere along their path to find the effective emission temperature as a function of position on the sky $T_b(x, y)$ (the sky brightness distribution). Throughout this treatment we will assume that we are in the Rayleigh-Jeans portion of the spectrum, so that the intensity B_ν is proportional to the brightness temperature T_b.

We find $T_b(x, y)$ by tracing the ray which intercepts the N^{th} (topmost) layer of the atmosphere at plane-of-sky position x, y downward through the layers until it either strikes the surface, or passes out of the back of the atmosphere. The technique is similar in many ways to those described in Hase and Höpfner (1999). The model uses cartesian coordinates x, y, and z, with the center of Venus at the origin, and the observer along the z-axis (at $z = \infty$). We define a ray as the set of points along a line:

$$\mathbf{r}(s) = \mathbf{a} + \mathbf{b}\, s \quad , \tag{10}$$

where $\mathbf{a}$ is the vector position of the starting point of the ray, $\mathbf{b}$ is a unit vector in the direction of the ray, and s is the distance along the ray. So, at the beginning of the ray trace for sky position (x, y), we set $\mathbf{a}_N = (x_N, y_N, z_N)$, where $x_N = x, y_N = y$, and $z_N = \sqrt{r_N^2 - x^2 - y^2}$, with r_N the radius of the upper boundary of the uppermost layer. The direction of the initial ray is: $\mathbf{b}_N = (0, 0, -1)$. We then calculate the distance to the next layer, s_N by performing a ray-sphere intersection test (see e.g., Haines 1989) with the sphere being defined by the radius of the lower boundary of the uppermost layer. The ray in the N^{th} layer is now all points along the ray with $s < s_N$. Appropriate quantities for that layer are then calculated (see below). The starting point of the ray in the next layer down (the $N - 1^{st}$ layer) is then defined by: $\mathbf{a}_{N-1} = \mathbf{a}_N + \mathbf{b}_N\, s_N$. To find the direction of the ray in the $N-1^{st}$ layer, we apply Snell's law, using the ratio of the indeces of refraction in the $N - 1^{st}$ and N^{th} layers. We do this following the method of Heckbert (1989), noting that the incident ray ($\mathbf{I}$ in Heckbert) is $\mathbf{b}_N$, and the surface normal ($\mathbf{N}$ in Heckbert) is $\mathbf{a}_{N-1}/|\mathbf{a}_{N-1}|$. This procedure is repeated down through the layers, yielding the ray parameters for each layer: $\mathbf{a}_i$, $\mathbf{b}_i$, and s_i for layer i. The ray trace is continued down through the layers until either the surface of the planet is intersected, or the ray-sphere intersection indicates that the lower boundary of a layer is not intercepted. If the lower boundary is not intercepted, we know that this is a limb-sounding ray. In that case, a ray-sphere intersection is performed with the sphere being defined by the radius of the upper boundary of the layer. In order to test whether the ray intersects the surface or not, in each layer with radius below the maximum topographic radius measured by Magellan, a surface intersection test is done, based upon the topography at the longitude and latitude along the ray in that layer. If the surface is intersected in level l, then s_l is set as the distance from $\mathbf{a}_l$ to the surface intersection point. The topography as a function of position is taken from the Magellan GTDR data set (Plautt 1993).

For rays which strike the surface, the brightness temperature is composed of three ele-

ments:

$$T_b(x,y) = T_{atm}(x,y) + T_{emit}(x,y) + T_{refl}(x,y) \quad , \tag{11}$$

where T_{atm} is the atmospheric contribution to the emission, T_{emit} is the surface emission contribution, and T_{refl} is the contribution due to downward atmospheric emission which is reflected back up by the surface. The atmospheric term is a sum of the contribution from each atmospheric layer, attenuated by the opacity of all layers above it. This can be written:

$$T_{atm}(x,y) = \sum_{i=l}^{N} T_i(\gamma_i, \phi_i) \left(1 - e^{-\tau_{i,i}}\right) \; e^{-\tau_{i+1,N}} \quad , \tag{12}$$

where l is the layer in which surface intersection occurs, T_i is the average physical temperature of the i^{th} layer (which can be a function of, e.g., latitude), γ_i and ϕ_i are the planetary longitude and latitude of the i^{th} layer, given x and y, and $\tau_{b,c}$ is an opacity term. The quantity $(1 - e^{-\tau_{i,i}}) \; e^{-\tau_{i+1,N}}$ is called the *weighting function* for layer i. The opacity term is:

$$\tau_{b,c} = \sum_{a=b}^{c} \tau'_a \quad . \tag{13}$$

The opacity of the i^{th} layer, τ'_i, is obtained by integrating along the ray in the layer ($\mathbf{r}_i(s) = \mathbf{a}_i + \mathbf{b}_i \, s$):

$$\tau'_i = \int_0^{s_i} k(s) \, ds \quad , \tag{14}$$

where $k(s)$ is the total atmospheric absorption at position s along the ray. This integral equation for the opacity in each layer is solved numerically. Note that it could be solved analytically if all of the contributions to the absorption were simple power laws in pressure and temperature for a given frequency, but this is not necessarily the case in the most general treatment of the problem. The absorption is a sum over all species which contribute to the microwave opacity, which we here assume are only CO_2, SO_2, and H_2SO_4. We use the expression of Ho *et al.* (1966) for the absorption of CO_2 (in units of km^{-1}):

$$k_{CO_2} = 2.65 \times 10^7 \; \nu_{GHz}^2 \; P^2 \; \left(\frac{1}{T}\right)^5 \; \left(f_{CO_2}^2 + 0.25 f_{CO_2} f_{N_2} + 0.0054 f_{N_2}^2\right) \quad , \tag{15}$$

where ν_{GHz} is the frequency in GHz, P is the pressure in atm, T is the temperature in K, f_{CO_2} is the molar fraction of CO_2, and f_{N_2} is the molar fraction of N_2. We use the expression of Kolodner and Steffes (1998) for the absorption of H_2SO_4, with a slight modification of the coefficient (again in units of km^{-1}):

$$k_{H_2SO_4} = 2.176 \times 10^9 \; \nu_{GHz}^{1.15} \; P^{1.08} \; \left(\frac{1}{T}\right)^3 \; f_{H_2SO_4} \quad , \tag{16}$$

where $f_{H_2SO_4}$ is the molar fraction of H_2SO_4. We use the full formalism of Suleiman *et al.* (1996) for the absorption of SO_2, including 1587 lines of SO_2 below 750 GHz. All of these absorptions require knowledge of the temperature and pressure along the ray path. We assume that temperature varies linearly in the layers, and that pressure varies exponentially, allowing us to calculate these quantities at each point along the path.

We combine the contributions from the surface and subsurface emission and surface reflection of downward emission from the atmosphere into one term:

$$T_{emit}(x,y) + T_{refl}(x,y) = T'_s(\gamma_l, \phi_l)\ e^{-\tau_{l,N}} \quad , \tag{17}$$

where T'_s is the *effective* brightness temperature of the surface at the appropriate latitude and longitude. Again, this is a combination of surface and subsurface emission and reflection:

$$T'_s(\gamma_l, \phi_l) = R(\gamma_l, \phi_l)\, T'_{\rm down}(x,y) + T''_s(\gamma_l, \phi_l) \quad , \tag{18}$$

where $R(\gamma_l, \phi_l)$ is the Fresnel reflectivity of the surface at the wavelength of interest for the surface location where intersection occurs, $T'_{\rm down}(x,y)$ is the effective brightness temperature of the downward atmospheric radiation, and $T''_s(\gamma_l, \phi_l)$ is the effective brightness temperature resulting from the emission from the surface and subsurface for the given surface location. We use a two layer subsurface model for the surface and subsurface emission (Warnock and Dickel 1972; Tikhonova and Troitskii 1969):

$$T''_s = \left(1 - R - R_2\, e^{-2\,\kappa\, a\, \sec e}\right)\ \left[T_s + \frac{q}{k\,\kappa\,\sec e'}\ \left(1 - e^{-\kappa\, a\, \sec e'}\right)\right] \quad , \tag{19}$$

where R_2 is the Fresnel reflectivity between the upper and lower subsurface layers, a is the depth of the upper layer, κ and k are the absorption coefficient and thermal conductivity in the upper layer, q is the heat flux from the interior of the planet, e is the emission angle from the upper layer into the atmosphere, e' is the emission angle from the lower layer into the upper layer, and T_s is the physical surface temperature. Note that the full model of Tikhonova and Troitskii (1969) allows for an additional term in this equation involving the diurnal subsurface temperature gradient in the upper layer. Given the thermal insulation of the atmosphere, it is expected that the this gradient should be very small on Venus, and that term has therefore not been included here. Note also that R, R_2, e, e', and T_s are all functions of the surface location where ray intersection occurs. The surface temperature, T_s, is calculated based upon the topography at the location where the ray strikes the surface, and the temperature vs. radius information input to the model. The absorption coefficient (κ) is defined by:

$$\kappa = \frac{2\,\pi}{\lambda}\ \tan\delta'\ \sqrt{\epsilon_r} \quad , \tag{20}$$

where ϵ_r is the real part of the complex dielectric constant of the upper layer (which we take as equal to the real part of the surface dielectric), and $\tan\delta'$ is the "specific loss tangent":

$$\tan\delta' = \frac{\tan\delta}{\rho\ (1-\omega)} = \frac{\epsilon_i/\epsilon_r}{\rho\ (1-\omega)} \quad , \tag{21}$$

where ρ is the density in the upper layer, ω accounts for scattering losses in the upper layer, ϵ_i is the imaginary part of the complex dielectric constant in the upper layer, and $\tan\delta$ is the loss tangent ($\tan\delta = \epsilon_i/\epsilon_r$).

The surface reflectivity is (by averaging the reflectivities in the parallel (p) and perpendicular (s) polarizations):

$$R = \frac{|r_p|^2 + |r_s|^2}{2} \quad , \tag{22}$$

where r_q is the reflection coefficient for polarization q. These reflection coefficients are:

$$r_p = \frac{-n^2 \cos e + \sqrt{n^2 - \sin^2 e}}{n^2 \cos e + \sqrt{n^2 - \sin^2 e}} \quad , \tag{23}$$

and

$$r_s = \frac{\cos e - \sqrt{n^2 - \sin^2 e}}{\cos e + \sqrt{n^2 - \sin^2 e}} \quad , \tag{24}$$

where n is the ratio of the index of refraction of the surface material to the index of refraction of the lowest atmospheric layer ($n \sim \sqrt{\epsilon_r}$ for a non-magnetic surface), and e is the emission angle (the angle between the incident ray and the surface normal). The real part of the dielectric constant of a surface with Fresnel reflectivity at normal incidence R_o is:

$$\epsilon_r = \left(\frac{1 + \sqrt{R_o}}{1 - \sqrt{R_o}} \right)^2 \quad . \tag{25}$$

The value of R_o as a function of location on Venus is taken from the GREDR data set (Plautt 1993).

The effective brightness temperature of the downward atmospheric radiation is given by:

$$T'_{\rm down} = T_{CMB}\ e^{-\tau_{l,N}} + \sum_{i=l}^{N} T_i(\gamma_i, \phi_i)\ \left(1 - e^{-\tau_{i,i}}\right)\ e^{-\tau_{l,i-1}} \quad , \tag{26}$$

where T_{CMB} is the cosmic microwave background temperature, taken to be 2.7 K.

For rays which do not strike the surface (limb sounding rays), the effective brightness temperature is composed only of atmospheric elements:

$$T_b(x, y) = T_{atm}(x, y) + T'_{atm}(x, y) \quad , \tag{27}$$

where the first term is the same as for the rays which strike the surface (Eq. 12), and the second term accounts for the emission from the back side of the atmosphere. This back side contribution is:

$$T'_{atm}(x, y) = \sum_{i=l}^{N} T_i(\gamma_i, \phi_i)\ \left(1 - e^{-\tau_{i,i}}\right)\ e^{-\left(\tau_{l,N} + \tau_{l,i-1}\right)} \quad . \tag{28}$$

Note that care must be taken in treating the lowest layer correctly. We do this by taking the ray through that layer, and dividing it in two, and taking the radius of that halfway point along the ray as the lower radius of the lowest layer. The average temperature of that lowest layer is then adjusted appropriately (assuming linear temperature variation).

The required inputs to the model are quantities as a function of altitude for the atmosphere, and values for the surface quantities as a function of position on Venus. As previously stated, the surface quantities (topography and dielectric constant) are taken from the GTDR and GREDR Magellan data sets (Plautt 1993). The necessary atmospheric quantities are:

pressure, temperature, and the molar fraction of the atmospheric constituents (CO_2, N_2, SO_2, H_2SO_4). Given the other inputs, the index of refraction is calculated in each layer via:

$$n_i = 1.0 + 0.1329 \, \frac{P}{T} \quad . \tag{29}$$

Given the ability to calculate the brightness temperature as a function of position, the average brightness temperature is then obtained by integration over the sky coordinates (see Eq. 3). It is common to assume azimuthal symmetry, reducing Eq. 3 to:

$$\overline{T_b} = 2 \int_0^1 T_b(\rho) \, \rho \, d\rho \quad , \tag{30}$$

for radial coordinate $\rho = r/R$. We do not take this step, in order to take into account the variations in the surface and atmospheric properties across the disk. We solve the full 2-D integral in Eq. 3 numerically.

Appendix B

In this appendix we derive the correction due to resolution of Venus in the primary beam of the antennas of the VLA. The theoretical antenna response of the VLA is circularly symmetric, and is given by (Napier, 1999):

$$A(u) = |F(u)|^2 \quad , \tag{31}$$

where:

$$F(u) = \frac{J_1(2\pi a u)}{\pi \, a \, u} \quad . \tag{32}$$

J_1 is the Bessel function of the first kind, order 1, a is the physical radius of the antenna (in meters), and u is the angle on the sky in wavelengths, i.e., $u = \theta/\lambda$, for sky distance θ in radians, and wavelength λ. For this theoretical primary beam, the full width half maximum (FWHM) as a function of wavelength is given by:

$$\theta_A = \frac{1.03 \, \lambda}{2 \, a} \text{ radians} \quad \sim \frac{42.42}{\nu_{GHz}} \text{ arcmin} \quad , \tag{33}$$

where ν_{GHz} is the frequency in GHz. The measured FWHM of the VLA antennas is well described by this relation. Using the data of Napier and Rots (1982), and fitting a primary beam like equation 32 for the FWHM yields $\theta_A \sim 44.43/\nu_{GHz}$. Note that Napier and Rots (1982) derive $\theta_A \sim 44.26/\nu_{GHz}$, but use a polynomial approximation to the primary beam shape rather than the more accurate Besselian shape. Table B.I shows the value of θ_A calculated using equation 33 for the wavelengths of our observations. This table also shows ← **Tab. B.I**

the size of the planet during our observations. It is apparent that some reduction in the detected flux density may occur due to resolution of Venus by the primary beam. We wish to correct for that reduction by calculating a correction factor, C, such that the *true* flux density (S_ν, see equation 2) is related to the *detected* flux density (S'_ν) by:

$$S_\nu = \frac{S'_\nu}{C} \quad . \tag{34}$$

So, given an observed source large enough such that $A(u)$ is significantly < 1 over some part of it, what is the reduction in flux density for a VLA antenna? Assuming circular symmetry, the ratio of the detected to true flux density is:

$$C = \frac{S'_\nu}{S_\nu} = \frac{\int_0^{u_{max}} A(u)\, B(u)\, u\, du}{\int_0^{u_{max}} B(u)\, u\, du} \quad , \tag{35}$$

where $B(u)$ is the source brightness distribution (assumed circularly symmetric), and u_{max} is the source size in wavelengths, i.e., $u_{max} = R/\lambda$ for a source of angular radius R. For the source distribution presented in the Deriving the Brightness Temperature section above ($B(u) = B_o \cos^n(u/u_{max})$), this becomes:

$$C = (2+n)\left(\frac{\lambda}{R}\right)^2 \int_0^{R/\lambda} A(u)\, \cos^n\!\left(\frac{u\lambda}{R}\right) u\, du \quad . \tag{36}$$

Unfortunately this integral must be evaluated numerically. Table B.I shows the resultant modified correction factor, expressed as a percent change in the flux density (i.e., $C' = 100\,(1-C)\,\%$), given the value of n derived from the fits. Also shown in Table B.I are values of C' calculated using $n = 0$ and $n = 1$, to illustrate that the value of C' (and C) is not particularly sensitive to variations in n, for our observations. Inspection of Table B.I shows that the correction is only $> 1\%$ for the highest frequency (22.46 GHz). However, since we know what the correction factor should be we still apply it at the longer wavelengths, even though the it is $< 1\%$. The exception is at the two longest wavelengths, where the correction is negligibly small (hence their exclusion from the table).

References

Allen, D.A., and J.W. Crawford 1984. Cloud Structure on the Dark Side of Venus. *Nature* **307**, 222–224.

Baars, J.W.M., R. Genzel, I.I.K. Pauliny–Toth, and A. Witzel 1977. The Absolute Spectrum of Cas A; An Accurate Flux Density Scale and a Set of Secondary Calibrators. *Astron. Astrophys.* **61**, 99–106.

Barrett, A.H. 1961. Microwave Absorption and Emission in the Atmosphere of Venus. *Astrophys. J.* **133**, 281–293.

Barrett, A.H., and D.H. Staelin 1964. Radio Observations of Venus and the Interpretations. *Space Sci. Rev.* **3**, 109–135.

Berge, G.L., and E.W. Greisen 1969. High–Resolution Interferometry of Venus at 3.12–cm Wavelength. *Astrophys. J.* **156**, 1125–1134.

Berge, G.L., D.O. Muhleman, and G.S. Orton 1972. High Resolution Interferometric Observations of Venus at Three Radio Wavelengths. *Icarus* **17**, 675–681.

Bézard, B., C. deBergh, B. Fegley, J.-P. Maillard, D. Crisp, T. Owen, J.B. Pollack, and D. Grinspoon 1993. The Abundance of Sulfur Dioxide Below the Clouds of Venus. *Geophys. Res. Lett.* **20**, 1587–1590.

Blamont, J., L. Boloh, V. Kerzhanovich, L. Kogan, M. Kurgansky, V. Linkin, L. Matveenko, M. Roy, D. Patsaev, *et al.* 1993. Balloons on Planet Venus – Final Results. *Adv. Space Res.* **13**, 145–152.

Butler, B.J., and T.S. Bastian 1999. Solar System Objects. In *Synthesis Imaging in Radio Astronomy II* (G.B. Taylor, C.L. Carilli, and R. A. Perley, Eds.) pp. 625–656. Astronomical Society of the Pacific Conference Series, San Francisco.

Campbell, M.J., and J. Ulrichs 1969. Electrical properties of rocks and their significance for lunar radar observations. *J. Geophys. Res.* **156**, 1125–1134.

Clark, B.G., and C.L. Spencer 1964. Some Decimeter Observations of Venus During the 1962 Conjunction. *Astron. J.* **69**, 59–61.

Clark, B.G., and A.D. Kuz'min 1965. The Measurement of the Polarization and Brightness Distribution of Venus at 10.6–cm Wavelength. *Astrophys. J.* **142**, 23–44.

Condon, J.J., D.L. Jauncey, and M.J. Yerbury 1973. The Brightness Temperature of Venus at 70 Centimeters. *Astrophys. J.* **183**, 1075–1080.

Cornwell, T.J., and E.B. Fomalont 1999. Self–Calibration. In *Synthesis Imaging in Radio Astronomy II* (G.B. Taylor, C.L. Carilli, and R. A. Perley, Eds.) pp. 187–199. Astronomical Society of the Pacific Conference Series, San Francisco.

Crisp, D., D.A. Allen, D.H. Grinspoon, and J.B. Pollack 1991. The Dark Side of Venus: Near Infrared Images and Spectra from the Anglo–Australian Observatory. *Science* **253**, 1263–1266.

Esposito, L.W., M. Copley, R. Eckert, L. Gates, A.I.F. Stewart, and H. Worden 1988. Sulfur Dioxide at the Venus Cloud Tops. 1978–1986, *J. Geophys. Res.* **93**, 5267–5276.

Fahd, A.K., and P.G. Steffes 1992. Laboratory Measurements of the Microwave and Millimeter–Wave Opacity of Gaseous Sulfur Dioxide (SO_2) under Simulated Conditions for the Venus Atmosphere. *Icarus* **97**, 200–210.

Florenskii, K.P., and 9 others 1982. Analysis of the Panoramas of the Venera 13 and Venera 14 Landing Sites. *Sov. Astron. Lett.* **8**, 233–234.

Ford, P.G., and G.H. Pettengill 1992. Venus Topography and Kilometer–Scale Slopes. *J. Geophys. Res.* **97**, 13103–13114.

Gurwell, M.A., D.O. Muhleman, K.P. Shah, G.L. Berge, D.J. Rudy, and A.W. Grossman 1995. Observations of the CO Bulge on Venus and Implications for Mesospheric Winds. *Icarus* **115**, 141–158.

Hall, R.W., and N.J.B.A. Branson 1971. High Resolution Radio Observations of the Planet Venus at a Wavelength of 6 cm. *Mon. Not. Roy. Astron. Soc.* **151**, 185–196.

Haines, E. 1989. Essential Ray Tracing Algorithms. In *An Introduction to Ray Tracing* (A.S. Glassner, Ed.) pp. 33–77. Academic Press, New York.

Hase, F., and M. Höpfner 1999. Atmospheric Ray Path Modeling for Radiative Transfer Algorithms. *Appl. Opt.* **38**, 3129–3133.

Heckbert, P.S. 1989. Writing a Ray Tracer. In *An Introduction to Ray Tracing* (A.S. Glassner, Ed.) pp. 263–293. Academic Press, New York.

Ho, W., I.A. Kaufman, and P. Thaddeus 1966. Laboratory Measurement of Microwave Absorption in Models of the Atmosphere of Venus. *J. Geophys. Res.* **71**, 5091–5108.

Janssen, M.A., and M.J. Klein 1981. Constraints on the Composition of the Venus Atmosphere from Microwave Measurements near 1.35 cm Wavelength. *Icarus* **46**, 58–69.

Jenkins, J.M., and P.G. Steffes 1991. Results for 13–cm Absorptivity and H_2SO_4 Abundance Profiles from the Season 10 (1986) Pioneer Venus Orbiter Radio Occultation Experiment. *Icarus* **90**, 129–138.

Jenkins, J.M., P.G. Steffes, D.P. Hinson, J.D. Twicken, and G.L. Tyler 1994. Radio Occultation Studies of the Venus Atmosphere with the Magellan Spacecraft 2. Results from the October 1991 Experiments. *Icarus* **110**, 79–94.

Jenkins, J.M., B.J. Butler, P.G. Steffes, and M.A. Kolodner 1998. Retrievals of Sulfur–Bearing Gas Abundances from Microwave Emission Maps of Venus Obtained at the VLA. *BAAS* **30**, 1449.

Kolodner, M.A., and P.G. Steffes 1998. The Microwave Absorption and Abundance of Sulfuric Acid Vapor in the Venus Atmosphere based on New Laboratory Measurements. *Icarus* **132**, 151–169.

Langseth, M.G., S.J. Keihm, and K. Peters 1976. Revised lunar heat-flow values, *Proc. Lunar Sci. Conf. 7th*, **7**, 3143–3171.

Lecacheux, L., P. Drossart, P. Laques, F. Deladerrière, and F. Colas 1993. Detection of the Surface fo Venus at 1.0 μm from Ground–Based Observations. *Planet. Space Sci.* **41**, 543–549.

McGovern, P.J., M. Simons, and S.C. Solomon 1995. Estimates of Elastic Lithosphere Thickness and Heat Flux Beneath Large Volcanoes on Venus. *LPSC XXVI*, 941–942.

Mitchell, D.L., and I. de Pater 1994. Microwave imaging of Mercury's thermal emission at wavelengths from 0.3 to 20.5 cm. *Icarus* **110**. 2–32.

Moore, H.J., J.M. Boyce, G.G. Schaber, and D.H. Scott 1980. Lunar remote sensing and measurements. *U.S. Geological Survey Prof. Paper 1046-B.*

Muhleman, D.O., G.L. Berge, and G.S. Orton 1973. The Brightness Temperature of Venus and the Absolute Flux–Density Scale at 608 MHz, *Astrophys. J.* **183**. 1081–1085.

Muhleman, D.O., G.S. Orton, and G.L. Berge 1979. A Model of the Venus Atmosphere from Radio, Radar, and Occultation Observations. *Astrophys. J.* **234**, 733–745.

Na, C.Y., L.W. Esposito, and T.E. Skinner 1990. International Ultraviolet Explorer Observation of Venus SO_2 and SO. *J. Geophys. Res.* **95**, 7485–7491.

Na, C.Y., L.W. Esposito, W.E. McClintock, and C.A. Barth 1994. Sulfur Dioxide in the Atmosphere of Venus II. Modeling Results. *Icarus* **112**, 389–395.

Napier, P. 1999. The Primary Antenna Elements. In *Synthesis Imaging in Radio Astronomy II* (G.B. Taylor, C.L. Carilli, and R.A. Perley, Eds.) pp. 37–56. Astronomical Society of the Pacific Conference Series, San Francisco.

Napier, P., and A. Rots 1982. VLA Primary Beam Parameters. VLA Test Memo No. 134, NRAO.

Oyama, V.I., G.C. Carle, J. Woeller, J.B. Pollack, R.T. Reynolds, and R.A. Craig 1980. Pioneer Venus Gas Chromotography of the Lower Atmosphere of Venus. *J. Geophys. Res.* **85**, 7891–7902.

Pettengill, G.H., P.G. Ford, and B.D. Chapman 1988. Venus: Surface Electromagnetic Properties. *J. Geophys. Res.* **93**, 14881–14892.

Pettengill, G.H., P.G. Ford, W.T.K. Johnson, R.K. Raney, and L.A. Sauderblom 1991. Magellan: Radar Performance and Data Products. *Science* **252**, 260–265.

Pettengill, G.H., P.G. Ford, and R.J. Wilt 1992. Venus Surface Radiothermal Emission as Observed by Magellan. *J. Geophys. Res.* **97**, 13091–13102.

Plautt, J.J. 1993. The Non–SAR Experiments. In *Guide to Magellan Image Interpretation* pp. 19–31, JPL Publication 93–24.

Saunders, R.S., *et al.* 1992. Magellan Mission Summary. *J. Geophys. Res.* **97**, 13067–13090.

Schloerb, F.P., D.O. Muhleman, and G.L. Berge 1976. Lunar Heat Flow and Regolith Structure Inferred from Intererometric Observations at a Wavelength of 49.3 cm. *Icarus* **29**, 329–341.

Sieff, A. 1991. Atmospheres of Earth, Mars, and Venus, as Defined by Entry Probe Experiments. *J. Space. Rock.* **28**, 265–275.

Sinclair, A.C.E., J.P. Basart, D. Buhl, and W.A. Gale 1972. Precision Interferometric Observations of Venus at 11.1–Centimeter Wavelength. *Astrophys. J.* **175**, 555–572.

Steffes, P.G., M.J. Klein, and J.M. Jenkins 1990. Observations of the Microwave Emission of Venus from 1.3 to 3.6 cm. *Icarus* **84**, 83–92.

Steffes, P.G., J.M. Jenkins, R.S. Austin, S.W. Asmar, D.T. Lyons, E.H. Seale, and G.L. Tyler 1994. Radio Occultation Studies of the Venus Atmosphere with the Magellan Spacecraft 1. Experimental Description and Performance. *Icarus* **110**, 71–78.

Suleiman, S.H., M.A. Kolodner, and P.G. Steffes 1996. Laboratory Measurement of the Temperature Dependence of Gaseous Sulfur Dioxide (SO_2) Microwave Absorption with Application to the Venus Atmosphere. *J. Geophys. Res.* **101**, 4623–4635.

Thompson, A.R., J.M. Moran, and G.W. Swenson Jr. 1991. *Interferometry and Synthesis in Radio Astronomy*, Krieger Publishing Co., Malabar.

Tikhonova, T.V., and V.S. Troitskii 1969. Effect of Heat from Within the Moon on its Radio Emission for the Case of Lunar Properties which Vary with Depth. *Sov. Astron. AJ* **13**, 120–128.

Turegano. J.A., and M.J. Klein 1980. Calibration Radio Sources for Radio Astronomy: Precision Flux Density Measurements at 8420 MHz. *Astron. Astrophys.* **86**, 46–49.

Tyler, G.L., R.A. Simpson, M.J. Maurer, and E. Holmann 1992. Scattering Properties of the Venusian Surface: Preliminary Results from Magellan. *J. Geophys. Res.* **97**, 13115–13139.

Ulich, B.L., J.H. Davis, P.J. Rhodes, and J.M. Hollis 1980. Absolute Brightness Temperature Measurements at 3.5 mm Wavelength. *IEEE Trans. Ant. Prop.* **28**, 367–377.

Vinogradov, A.P., K.P. Florenskii, A.T. Bazilevskii, and A.S. Selivanov 1976. First panoramic pictures of Venus: preliminary image analysis. *Sov. Astron. Lett.* **2**, 67–71.

Warnock, W.W., and J.R. Dickel 1972. Venus: Measurements of Brightness Temperatures in the 7-15 cm Wavelength Range and Theoretical Radio and Radar Spectra for a Two-layer Subsurface Model, *Icarus* **17**, 682–691.

Watkins, J.S., and R.L. Kovach 1974. Seismic Investigation of the Lunar Regolith, *Proc. Lunar Sci. Conf. 4th*, **7**, 2561–2574.

Zasova, L.V., V.I. Moroz, L.W. Esposito, and C.Y. Na 1993. SO_2 in the Middle Atmosphere of Venus: IR Measurements from Venera–15 and Comparison to UV Data. *Icarus* **105**, 92–109.

Table I. Ephemeris information for Venus observations.

date	time range (IAT)	RA	Dec	D (AU)	phase angle	sub-Earth lon,lat (deg)	frequencies (GHz)
April 05, 1996	1645–2747	03:57:16.65	+24:04:23.2	0.6735	92	216.5,-4.6	14.94, 22.46
April 30, 1996	0148–0224	05:21:46.50	+27:39:02.8	0.4862	112	271.6,-5.3	4.86, 8.44
January 21, 1999	1710–1850	21:37:02.54	-15:52:18.3	1.5670	28	187.9,1.1	1.465, 1.385

Table II. Calibrators.

date	frequency (GHz)	3C286 flux density (Jy)	secondary calibrator, flux density (Jy)
April 05, 1996	22.46	2.50	0403+260, 0.56
April 05, 1996	14.94	3.43	0403+260, 0.64
April 30, 1996	8.44	5.19	0555+398, 5.94
April 30, 1996	4.86	7.49	0555+398, 5.95
January 21, 1999	1.465	14.51	2131-121, 1.84
January 21, 1999	1.385	14.90	2131-121, 1.83

Table III. Fit values.

frequency (GHz)	V_o (Jy)	$\overline{T_b}^a$ (K)	n
22.46	88.860 ± 0.004	505.2 ± 25.3	0.161
14.94	44.454 ± 0.001	565.9 ± 17.0	0.151
8.44	31.736 ± 0.002	657.5 ± 13.2	0.096
4.86	10.915 ± 0.001	679.9 ± 13.6	0.019
1.465	0.08699 ± 0.0003	619.0 ± 12.4	0.035
1.385	0.07702 ± 0.0003	612.8 ± 12.3	0.035

[a] includes primary beam correction (see appendix B), and uncertainty in flux density calibration scale.

Table B.I. Correction factors for primary beam resolution.

frequency (GHz)	θ_{venus} (arcsec)	θ_A (arcsec)	C' (%)	$C'(n=0)$ (%)	$C'(n=1)$ (%)
22.46	25.1	120	1.57	1.60	1.44
14.94	25.1	180	0.69	0.71	0.63
8.44	34.7	320	0.44	0.44	0.40
4.86	34.7	550	0.15	0.15	0.13

Table IV. Example model runs.

frequency (GHz)	measured $\overline{T_b}$ (K)	Model temp profile SO_2 (ppm) H_2SO_4 (ppm) subsurface?	a PV 130 4.8 yes	b PV 130 0 yes	c PV 40 0 yes	d PV 0 0 yes	e MV 130 4.8 yes	f MV 40 4.8 yes	g MV 40 2.4 yes	h MV 40 0 yes	i MV 40 2.4 no	j MV 40 2.4 yes[a]
22.46	505.2 ± 25.3		469.5	487.0	502.4	510.6	472.8	486.5	499.0	513.3	499.0	499.0
14.94	565.9 ± 17.0		524.5	542.9	558.4	566.5	534.2	548.8	561.8	575.8	560.7	560.7
8.44	657.5 ± 13.2		610.2	626.0	637.7	643.2	624.4	635.3	645.7	656.5	633.8	634.2
4.86	679.9 ± 13.6		666.6	676.9	681.0	682.8	677.9	680.5	687.6	694.2	654.2	655.4
1.385	612.8 ± 12.3		674.7	676.4	675.7	675.5	684.5	684.1	685.2	686.0	618.0	620.2
		χ_r	10.9	4.05	1.23	0.63	5.72	2.19	0.62	0.78	3.47	3.25

[a] modified subsurface thermal conductivity - see text.

B.J. Butler *et al.* – Figure 1.

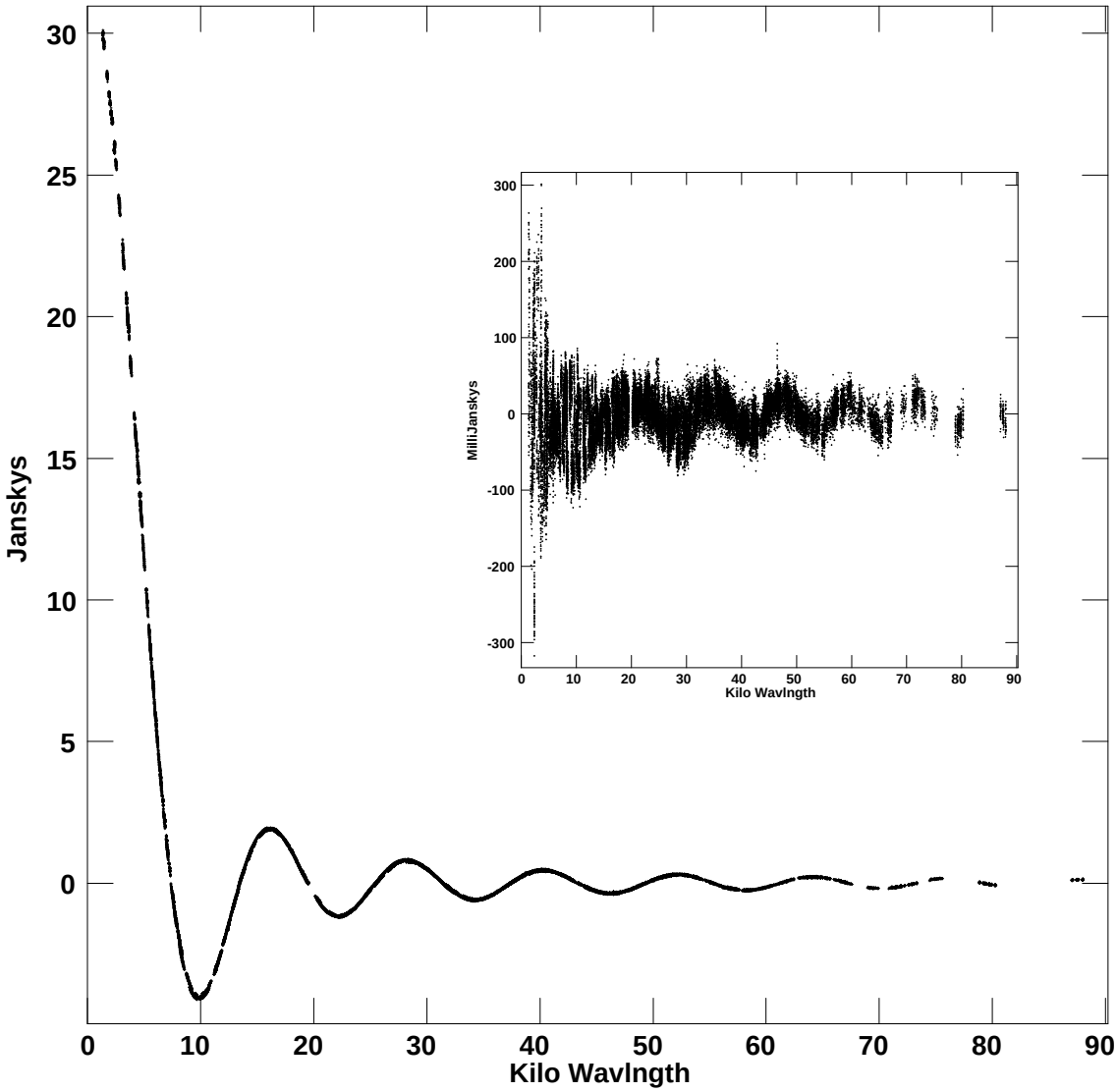

Figure 1. Measured visibilities from Venus at 8.44 GHz as a function of baseline length (in wavelengths). Shown in the inset are the residuals after the best-fit circularly symmetric model was subtracted.

B.J. Butler *et al.* – Figure 2.

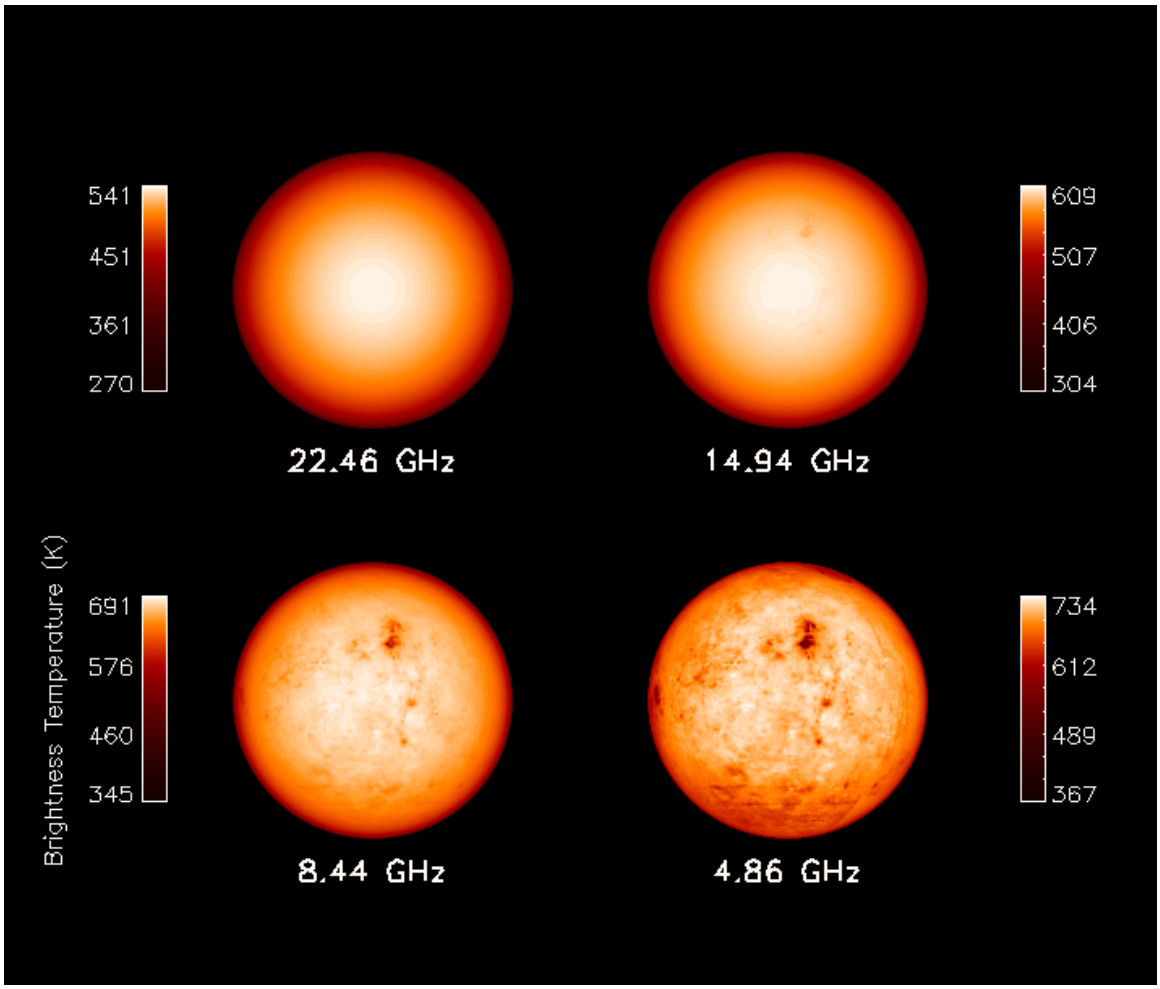

Figure 2. Maps of the model brightness temperature distributions at the four highest frequencies presented here.

B.J. Butler *et al.* – Figure 3.

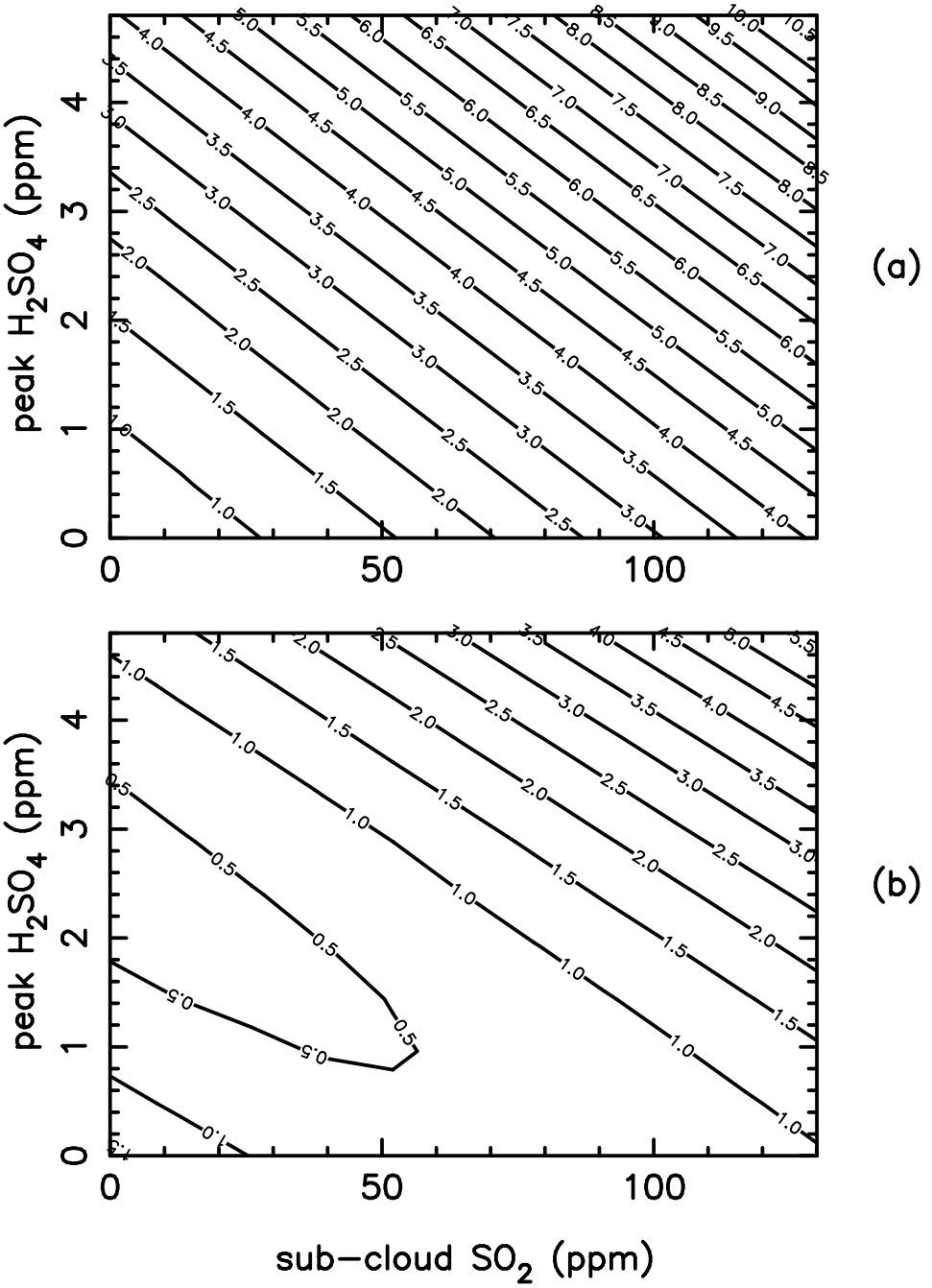

Figure 3. Plot of reduced chi-square for different amounts of sub-cloud SO_2 and peak H_2SO_4 abundance: (a) for the Pioneer-Venus sounder temperature profile (Sieff 1991); (b) for the extrapolated Mariner V occultation temperature profile (Muhleman *et al.* 1979).

B.J. Butler *et al.* – Figure 4.

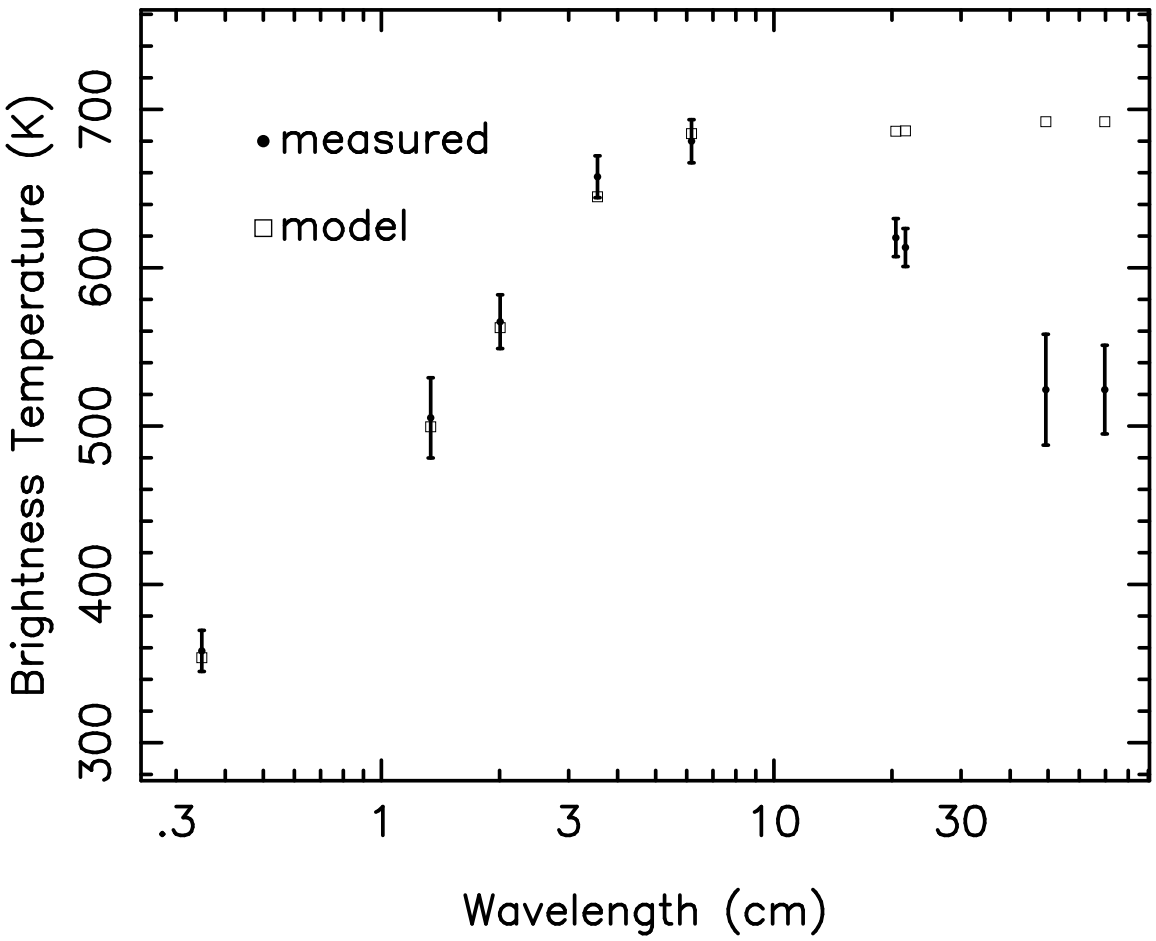

Figure 4. Derived disk averaged brightness temperature for Venus for the six wavelengths presented here, one additional short wavelength (Ulich *et al.* 1980), and two additional long wavelengths (Schloerb *et al.* 1976; Condon *et al.* 1973). Also shown are the model values at the same wavelengths for model (g) from Table IV.